

Ocean water clarity and the ocean general circulation

Anand Gnanadesikan and Whit G. Anderson

NOAA/Geophysical Fluid Dynamics Lab and Princeton University, Princeton, NJ

Manuscript in preparation for J. Phys. Oceanography

October 9, 2007

Abstract

Ocean water clarity affects the distribution of shortwave heating in the water column. In a one-dimensional time-mean sense, increased clarity would be expected to cool the surface and heat subsurface depths as shortwave radiation penetrates deeper into the water column. However, wind-driven upwelling and the seasonal cycle of mixing can bring water heated at depth back to the surface- warming the tropics and cooling the subtropics. This paper examines how these changes propagate through the climate system in a coupled model with an isopycnal ocean component to affect the general circulation of the ocean. A clear ocean has a stronger Hadley cell, weaker Walker cell, and midlatitude jet streams that shift equatorwards, with significant impacts on the subtropical gyres. The changes in wind stress also have an impact on the temperature structure at high latitudes, especially in the Southern Ocean, where they result in an increase in stratification, higher summertime temperatures, a shift in the watermasses involved in Antarctic Intermediate Water/Subantarctic Mode Water formation and a decrease in vertical exchange. The temperature changes responsible for this shift appear to be associated with extratropical chlorophyll. A striking impact is seen on the structure of the Mediterranean outflow, which shallows substantially as the water clarity increases. The resulting increase in near-surface salinity propagates to the north and acts to slightly increase the formation of North Atlantic Deep Water. The results highlight the potential ability of changes in nutrient supply to the oceans as well as mixing below the mixed layer to alter the general circulation.

Introduction

If ocean water were perfectly clear, solar radiation in the blue and near-UV bands would penetrate to great depths with e-folding scales exceeding 50m (Morel, 1988, Morel et al., 2007). In general, however, the depth of penetration is much shallower than this (Jerlov, 1969) due to the presence of phytoplankton pigments, colored dissolved organic matter, and scatterers such as plankton, bacteria, viruses and suspended particles. This paper asks the question of whether the anomalous shortwave absorption represented by these substances plays a significant role in determining the large-scale ocean circulation.

While a number of authors (Lewis et al., 1990; Stramska and Dickey, 1993) suggested that shortwave absorption could be important within a one-dimensional framework, large impacts have not generally been found in full three-dimensional models. Nakamoto et al. (2001), Sweeney et al. (2005) and Manizza et al. (2005) all looked at the impact of changing shortwave absorption profiles in ocean-only models. Increasing water clarity was found to increase the surface temperatures in the cold tongue by up to a degree, with very small changes in sea surface temperature away from this region. Sweeney et al. (2005) explained the mechanism behind such a change in terms of deeper mixed layer depths near the equator allowing more of the equatorial upwelling to be supplied from within the mixed layer. Shell et al. (2003) suggested that the initial response of the atmosphere should be to increase these temperature perturbations, as they would be expected to trigger Bjerknes-type feedbacks.

However, a result showing that the initial response to a climate perturbation will amplify does not necessarily imply that the long-term response will be large. As the El

Niño Southern Oscillation system shows, both positive and negative feedbacks act on changes in equatorial circulation. As a result, an El Niño-like perturbation will be damped out if the reduction in upwelling results in a decrease in the volume of light water (Federov et al., 2006).

The idea that ocean water clarity plays a small role in determining the circulation has received further support from the relatively small impacts seen in two lines of research with coupled climate models. One line, represented by Schneider and Zhu (1998), Christian et al., (2001), and Murtugudde et al. (2003) examines the impact of replacing a fixed attenuation scale with one based on observed chlorophyll using a hybrid coupled model. These papers allow for changes in the mean state of the ocean but ignore atmospheric thermodynamic feedbacks and, in general, find relatively small changes in such features as sea surface currents and overturning. Because of the spatial structure of the observed chlorophyll field, the perturbation that is used in these simulations results in a decrease in water clarity and shortwave penetration at the equator and an increase off-equator in the subtropical gyres. Legaigne et al. (2007) use a full coupled climate model and examine the difference between using prescribed and predicted chlorophyll concentrations. Relative to observations, their simulated chlorophyll fields also result in a decrease in penetration along the equator and an increase in penetration in the gyres.

The nature of the perturbation studied in these coupled models is significant, given the suggestions of mechanisms discussed in the ocean only models. In particular, the work of Sweeney et al. (2005) suggests that reducing shortwave penetration along the equator- insofar as it will act to reduce the depth of the mixed layers locally, will actually produce more upwelling and a *cooler* equator. Increasing water clarity and shortwave

penetration off equator, by contrast would be expected to result in *heating* the equatorial zone, as such water is upwelled along the equator. This suggests that all of the coupled simulations have greatly underestimated the impact of ocean water clarity on the large-scale circulation.

Confirmation of this was provided in recent work by Anderson et al. (2007), who examine the difference between pure water absorption and a scheme in which shortwave absorption is parameterized according to the observed chlorophyll concentration. The results show significant changes in sea surface temperature and winds, with the climate in the case without anomalous shortwave absorption shifting towards what would be a permanent El Nino in the control. Anderson et al. (2007) show that this shift is due to subsurface heating of water before it is entrained in the Equatorial Undercurrent. In two subsequent papers we extend this work to examine what these changes in water clarity can teach us about tropical variability (Anderson et al., 2007a) and tropical cyclogenesis (Anderson et al., 2007b).

This manuscript focuses on how changes in water clarity affect the general circulation of the ocean. In Section 2, we describe the coupled models used in this work. Section 3 discusses the simulated responses in the horizontal average temperature, salinity and age, the circulation of the subtropical gyres, overturning and watermass transformation within the Southern Ocean, changes in the Mediterranean outflow and Atlantic overturning. Section 4 discusses implications of this work.

2. Model Description

The atmospheric and land components of the model are identical to those used for the CM2.1 global coupled climate model developed for the Fourth Assessment Report of the Intergovernmental Panel on Climate Change and reported in Delworth et al. (2006). The atmosphere is built around a 24-level, 2x2.5 degree finite volume core with state-of-the-art representations of radiation, convection, and gravity wave drag. The land model is the LM2 model based on the work of Milly and Shmakin (2002), which fixes land properties such as albedo, surface roughness and stomatal resistance (which controls evapotranspiration) based on currently observed land types. The model has one of the better atmospheric simulations in the AR4 dataset (Reichler and Kim, *subm.*) and when coupled has been found to exhibit a reasonable simulation of El Nino and its feedbacks for both a level-coordinate ocean model (Van Oldenburgh et al., 2005) and an isopycnal ocean model (Anderson et al., 2007b).

The primary difference between these runs and those done for the Fourth Assessment report is the ocean model. The ocean model used in our simulations is the isopycnal layer model of Hallberg (2005). One key feature of this model is that it has essentially no numerical diapycnal mixing, allowing for clean attribution of changes in heat redistribution at depth (Harrison and Hallberg, 2007). Additionally, because the model uses a C-grid, in which velocities are computed on the faces of tracer cells, it is possible to represent narrow gaps such as the Straits of Gibraltar by limiting the area that connects adjacent cells, allowing us to resolve a 12km strait in a 1 degree model (Hallberg et al., *in prep.*). Finally, isopycnal models do not suffer from the excessive

entrainment of overflows associated with level coordinate models (Winton et al., 1998). The ability to resolve both narrow straits and overflows will be particularly important later in this paper. The model was configured with 48 interior isopycnal layers which strive to follow a set of target densities in addition to a four-layer mixed layer/buffer layer in which densities are free to vary. The model includes a nonlinear equation of state, and Richardson number dependent shear mixing. The impact of unresolved mesoscale eddies is parameterized using a biharmonic Smagorinsky viscosity and along-isopycnal mixing of both tracers and interface height (corresponding to the Gent and McWilliams, 1990 parameterization of eddy Stokes drift in level-coordinate models). A constant coefficient of $900 \text{ m}^2/\text{s}$ is used for both terms.

A key difference between the model used in these simulations and previous instantiations of the isopycnal model is that we incorporate the two-band shortwave penetration scheme of Manizza et al. (2005), which is a reanalysis of the data of Morel (1988) permitting very low chlorophyll concentrations. As our top mixed layer is always 10m deep our parameterization effectively takes the profile of light below this level as

$$(1a) \quad I(z) = I_{BG} e^{-k_{bg} z}$$

$$(1b) \quad k_{bg} = 0.0232 + 0.074 * chl^{0.674}$$

Where $I_{bg} = I_0 * 0.21$ (21% of the absorbed solar radiation is taken to be blue-green) and chl is the concentration of chlorophyll-a in $\text{mg chl}/\text{m}^3$. Thus if the chlorophyll is set to 0, blue-green light has an e-folding depth of 43m, while at values of $0.2 \text{ mg chl}/\text{m}^3$ it is about 20m. In the base state of the model, the chlorophyll concentrations are taken from the non-El Nino SeaWIFS climatology developed by Sweeney et al. (2005) that is

currently distributed with the GFDL ocean codes (Figure 1). This base state is referred to as the *Green* run.

The *Green* simulation is comparable to other models run as part of the AR4 process. The RMS sea surface temperature error (Figure 2a) from years 200-300 of the control run is 1.42 C, slightly less than GFDLs CM2.0 model and about 0.2C greater than the CM2.1 model (Table 1). An area of particular interest is the Pacific cold tongue, where the Green model has a small positive bias, in marked contrast to the strong negative biases in the CM2 series runs. The upper ocean temperature errors in the *Green* model (Figure 2b) are better than either of the two level coordinate models- particularly in the Atlantic. Salinity errors (Figure 2c,d) in the Green model are slightly worse than in the CM2 series, possibly because this model has not been subjected to exhaustive tests of how to mix freshwater into the interior at river mouths.

Several perturbations in ocean water clarity were performed. The first (*Blue*) was the largest possible, removing all anomalous shortwave absorption. The *Blue* model was run out for 300 years. Additionally, four additional 120 year runs were made in which the chlorophyll concentration was everywhere reduced by 50% (*Half*), set to zero when it was less than 0.2 mg/m³ (*Limit_0.2*), set to zero within 5 degrees of the equator (*Noequ*), and set to zero over the “shadow zones” defined as regions within 30 degrees of the equator in regions where the average chlorophyll is greater than 0.2 (*Shadow*). Interestingly, the shadow zones defined in this manner cover the oxygen minimum zones. The *Half* run thus can be used to evaluate the linearity of the system, the *Limit 0.2* run to evaluate the impact of clarity in the clear gyre centers, the *Noequ* run to evaluate the

impact of equatorial water clarity, and the *Shadow* run (particular when contrasted with the *Noequ* run) to evaluate the importance of water clarity over the shadow zones.

The perturbations we have made in these runs are quite large. This was done intentionally for two reasons. First, our experimental design enables us to set an upper limit on the impact of ocean color in different regions. More importantly, it allows us to produce signals that are large in comparison to the natural variability of the coupled system so that changes are much more likely to be statistically significant.

The ocean models were initialized from a modern January climatology based on the World Ocean Atlas dataset. The atmosphere was initialized with radiatively active trace gas concentrations set at 1990 level (thus corresponding to the 1990ctrl runs in the IPCC AR4 model database). The models all develop a very strong La Nina in the first 20 years, but afterwards are relatively stable. Unless otherwise specified, differences between the *Half*, *Limit_0.2*, *Limit_0.1*, *Shadow* and *Noequ* runs reported in this work are computed from years 41-120.

3. Results

a.) SST and wind stress changes

That ocean water clarity has an important impact on sea surface temperature and wind stress is clearly shown in Figure 3. The net impact of water clarity on SST (illustrated by the *Blue-Green* differences) is global in extent, with peak values exceeding 4C and RMS differences of 0.6C. The pattern shows a strong warming in the central Pacific, with cooling off-equator in the subtropical gyres (particularly in the Atlantic),

strong cooling at the boundary between the subtropical and subpolar gyres, and warming in the subpolar gyres. The wind stress changes associated with this have a complicated pattern. Increasing equatorward winds to the north and south of the equator in the central Pacific are associated with an increase in the Hadley circulation, while westerly anomalies along the equator correspond to a decrease in the Walker circulation. The northern jet stream shows a tendency to shift equatorwards. The southern jet stream shows some hint of a shift but also weakens significantly.

The magnitude of the response to changing chlorophyll is nonlinear, as might be expected from the exponential dependence of absorption. When the chlorophyll decreases by a factor of 2 (*Half* run, Figure 3b) the pattern of the response is reasonably similar to that produced by increasing water clarity everywhere (correlation coefficients are high globally and in the central Pacific) but the magnitude is significantly attenuated, reaching only 35-40% of that seen in Figure 3a. The wind stresses show similar changes in the equatorial region, but less of a change in the subpolar regions.

As discussed in Anderson et al. (2007) relatively little of the response can be explained by changes in water clarity right along the equator. The pattern of SST change in *Noequ* simulation (in which all the additional shortwave penetration occurs right on the equator, Figure 3c) is poorly correlated with the global *Blue-Green* difference. This is true even in the Central Pacific where the largest signals are seen. Essentially, the warming in the Eastern Pacific to the south of the equator is the only major feature reproduced. The magnitude of the SST response to changing near-equatorial shortwave penetration is quite small, of order 10% of the response to removing anomalous shortwave absorption everywhere.

By contrast, in the *Limit 0.2* run (in which the increased shortwave penetration occurs off-equator in the clear subtropical gyre centers, Figure 3d) a much more vigorous response with significantly higher correlation to the *Blue-Green* response is seen. This simulation reproduces the pattern of on-equatorial warming (though weakly) strong off-equatorial cooling and the shift of the gyre boundary in the North Pacific. The wind stress response, however is much more confined to the equator than in *Blue* and does not exhibit the westerly anomalies along the equator. Essentially, the Pacific branch of the Hadley cell appears to be sensitive to the water clarity in the gyres.

The *Shadow* simulation (in which the additional penetration occurs in the less-clear eastern portions of the basin, Figure 3e) shows a quite different pattern, with a general warming over most of the ocean, but particularly strongly in the eastern Pacific. The winds follow this warm anomaly, which results in an increase in the Southern Hadley cell and a strong westerly anomaly along the equator. The Walker circulation appears to be much more sensitive to water clarity above the oxygen minimum zones.

It is interesting to consider the extent to which the water clarity perturbations are linear, by adding the SST change between *Limit 0.2* and *Green* to that between *Shadow* and *Green*. The result (Figure 3f) is a pattern that has a very high correlation with *Blue-Green* in the Central Pacific where it reproduces not only most of the spatial pattern but about 85% of the magnitude. Globally, the correlation is significantly lower, as the large warming of the subpolar gyres and cooling of the Atlantic is not reproduced.

The water balance over the ocean also changes as the water clarity is changed (Figure 4). As with temperature, the basic pattern can be seen to consist of two main components. The first patterns, exemplified by *Limit 0.2*, involves increased penetration

in the clear gyre centers resulting in an increase in the Hadley cell (Figure 4d) producing lower salinities along the equator and higher salinities off equator in the center of the subtropical gyres. The other, exemplified by *Shadow* involves increased penetration above the oxygen minimum zones, producing a warming of the cold tongue and an eastward shift of the precipitation into the central Pacific, away from Indonesia. Interestingly, the salinity change associated with this perturbation is largely negative, with maximum freshening of ~ 0.6 PSU over the central Pacific. Notice that the zero line in SSS change for *Shadow-Green* does not correspond to the zero line in precipitation-evaporation change in *Blue-Green*, or *Limit 0.2- Green*. This difference highlights the importance of advection in smoothing out the impact of precipitation changes within a gyre.

b.) Zonal mean T,S, age

Having sketched out the changes in surface properties, we now consider how these changes affect the structure of the interior ocean. The basic picture in the tropics is one in which increasing penetration of solar radiation leads to a small net cooling of the surface and a large (up to 2.5C in the *Blue* run) warming between 100 and 400m (Figure 5a). These depths also become saltier (Figure 5c) and younger (Figure 5e). As with the surface temperatures, the *Half* run shows about $\frac{1}{4}$ of the signal in tropical temperature and salinity but exhibits an even smaller signal in age. The importance of shortwave penetration in the off-equatorial gyres is illustrated by the fact that the *Limit 0.2* run has a similar pattern of change between 200 and 400m in all three fields, although the

magnitude of the change is only 20-40% of that in the *Blue* run. Additionally, there is considerable penetration of warming below 400m, with the *Blue* run showing 0.6 C of warming at 600m. At these depths none of the runs with a low-latitude color perturbation shows much signal.

These deep changes may be linked to changes in the Southern Ocean. Examination of the temperature fields (Figure 5b) shows an increase in these same waters in the *Blue* run. Such changes are not seen in the other simulations, suggesting that high-latitude changes in water clarity may be important. The *Blue* run also has a significantly fresher surface Southern Ocean (Figure 5d) and a older mid-depth Southern Ocean with waters aging by up to 6 years (Figure 5f). Both *Limit 0.2* and *Shadow* show qualitatively similar patterns of change in salinity and age, with increasing Southern Ocean stratification in the mean. We will examine this issue in more detail in Section 3d when we consider Southern Ocean watermass formation.

c) Tropics and subtropical wind-driven circulation

The changes in sea surface temperatures associated with increasing water clarity (Figure 3) result in at least three major responses in the wind stress. The first is to increase convergence along the equator, effectively increasing the magnitude of the Hadley circulation and thus intensifying the zonal winds driven by this circulation. This can be seen most clearly in the *Limit 0.2* run and is associated with the clear gyre centers. Additionally, the changes in the upper-level winds produce changes in wave activity fluxes, shifting the eddy-driven jets in mid-latitudes equatorwards so that the steep

gradients in wind stress associated with the flanks of these jets intensify over the polar gyres. This effect is extremely pronounced over the subpolar North Pacific and Southern Ocean in the *Blue* run. Finally the shift in convection associated with the warming of the Eastern Equatorial Pacific (most clearly seen in Figure 2 of Anderson et al., 2007a) results in an El Nino-like wave pattern that has its expression in the intensification of the Aleutian Low and an intensification of the low pressure over the Amundsen Sea. This last change is most strongly associated with the changes in water clarity in the shadow zones.

These changes in winds produce substantial changes in the wind stress curl and thus in the Sverdrup transport. Figure 6b-f shows the changes in Sverdrup transport for *Blue-Green*, *NoEqu-Green*, *Half-Green*, *Limit 0.2-Green*, and *Shadow-Green* simulations, with Figure 6a showing the Sverdrup transport in the *Green* control case for comparison. As would be expected from Figure 3, the *Limit 0.2* changes are more confined to the tropics, while the other runs show changes in the extratropics. It is important to note that even a change of $0.4 \text{ m}^2/\text{s}$ (the smallest colored contour interval) will correspond to a change of about 5 Sv when integrated across the Pacific Ocean, so that the changes seen, though certainly smaller than the mean circulation, are nonetheless significant. The change in the barotropic streamfunction derived from integrating the horizontal velocity along 172E (Figure 7a) shows a significant increase in the transport associated with the North and South Equatorial Currents, and their return flow in the EUC.

Analysis of the differences in transport at 18N, 15S and 25S (Figures 7b-d) demonstrate that they can largely be attributed to the changes in Sverdrup transport. At 18N (Figure 7b), the changes are quite similar in shape for the four models, differing

primarily in magnitude, with the *Blue*, *Limit 0.2*, *Half* and *Shadow* cases producing increases in the gyre circulation of 16, 12, 6 and 2Sv respectively. In the first three runs, this can be attributed to an increase in the Hadley cell north of the equator, resulting in a strengthening of the peak easterlies to the north. In the *Shadow* run, by contrast, there is much less strengthening of the northern Hadley cell, and the impact is relatively weak. The changes at this latitude are thus dominated by the changes in the relatively clear gyres.

This is not the case, however, at 10S (Figure 7c). In the *Limit 0.2* case, the enhancement of the upwelling branch of the Hadley cell results in an increase and slight equatorward shift in the easterly jets to the north and south of the equator (though more so in the south than in the north). This in turn results in an equatorward shift of the subtropical gyre with an increase of 12 Sv in the gyre transport at 10S. In the *Shadow* case, by contrast, there is a decrease in the wind stress curl in the western Pacific, associated with the movement of the southern rain band to the east, resulting in an increase in the northward transport at this latitude. The *Blue* and *Half* cases show a mixture of these two results, predicting essentially no increase in the gyre transport. Not all of the response can be attributed to local changes in the winds- there is an offset of about 2Sv which is associated with a change in the Indonesian throughflow.

Moving further into the southern subtropics, we see that the dominant impact shifts to being from the high-chlorophyll regions (Figure 7d). At 25S, both the *Half* and *Limit 0.2* runs show a relatively small impact on wind stress curl and transport while *Shadow* and *Blue* show a strong increase in northward Sverdrup transport associated

with the eastward shift in precipitation (and the associated low pressure system) into the central Pacific.

c.) Southern Ocean, SAMW/AAIW Formation

Changes in wind stress magnitude and location over the Southern Ocean have been hypothesized to have the potential to cause significant changes in ocean ventilation and overturning (Toggweiler and Samuels, 1993,1998; Gnanadesikan and Hallberg, 2000; Toggweiler, Russell and Carson, 2006). This is especially true in low-diffusion models where wind-driven Southern Ocean upwelling represents the dominant pathway by which dense deep waters are transformed into lighter surface waters (Toggweiler and Samuels, 1998; Gnanadesikan, 1999). The large changes in wind stress magnitude in this region would thus be expected to produce significant changes in overturning circulation, as shown in Figure 8. The *Half*, *Limit_0.2*, and *Green* runs are essentially identical, with 18 Sv of light and 18-19 Sv of dense water entering the Southern Ocean and 6 Sv of abyssal and 30 Sv of intermediate and mode waters leaving the region. The *Blue* run is significantly different. The supply of light water associated with the subtropical gyres increase by almost 40% to 25 Sv. The northward flow of mode and intermediate waters also increases, to about 37 Sv. As a result the mode and intermediate waters even more dominated by the lighter watermass classes.

The fact that the overturning is so different for the *Blue* run raises the question of the role played by extratropical ocean color, which we have largely ignored until now. By trapping heat near the surface, extratropical solar absorption will tend to raise wintertime

temperatures while lowering summertime temperatures. Such a temperature change could have one of two impacts. First, it could have a direct impact on watermass transformation. In order to explain the changes seen here, we would expect that the *Green* run would have significantly more summertime transformation of dense water. Second, the changes in seasonal temperature could have an impact on the wind stress field, resulting in a change in the gyre circulation. Analysis of the transport of water lighter than 1034.5 (Figure 9a) shows that there is more creation of this water within the Southern Ocean throughout the year (suggesting that it is not the impact of temperature alone). Additionally, the location where the additional creation of light water occurs is aligned with the wind stress. The *Limit 0.2* and *Shadow* perturbations, when added together, do produce a slightly enhanced southward transport of this light water, but do not show the enhancement in northward transport (Figure 9b). Neither do these low latitude perturbations reproduce the relatively large changes in the wind stress (up to 0.03 Pa in the zonal mean in some months) or in SST (changes of up to 0.70C). This suggests that it is the indirect effect of extratropical temperature changes on the wind stress that is most important for changing the Southern Hemisphere overturning.

d.) Mediterranean outflow

A final region where significant changes are seen in the Mediterranean outflow region. On examining the spatial structure of temperature and salinity changes, one of the biggest surprises was the large changes observed at mid-depths in the Atlantic (Figure 10). Along the $\sigma_2=36.69$ surface, the *Blue* run is substantially fresher and cooler than the

Green near the Mediterranean outflow, while along the 35.77 surface it is significantly saltier. This change is the result of a significant shift in the outflow density and thus in the depth of the Mediterranean outflow, which is turn driven by changes in freshwater balance within the Mediterranean. As seen in Table 2, the net flux through Gibraltar changes from 0.032 Sv in the *Green* run to 0.015 Sv in the *Blue* run, implying a significant decrease in the net salinification of the Mediterranean basin. This arises from a change in the storm track, which brings more precipitation to central Europe and thus deposits more in the Black Sea. Transport in the Bosphorus in the *Blue* run is almost twice as large in the *Blue* run than in the *Green*, increasing from 0.011 Sv to 0.020 Sv. Increased flow in the Nile accounts for an additional 0.02 Sv and the remainder is due to increased precipitation and runoff throughout the Mediterranean basin. The *Limit 0.2* run, with its dominant impact in the Pacific, still shows significant changes in the Mediterranean with small changes in the salinity at depth, while the *Half* run has a smaller impact. The *Shadow* run, by contrast (not shown), has very little impact on the outflow or salinity structure in the Atlantic.

An issue that has concerned oceanographers over many decades is the role of the Mediterranean Sea in helping to drive the Atlantic overturning. Reid (1979) showed that high-salinity and high oxygen Mediterranean waters could be tracked across the Faeroe-Shetland channel into the Norwegian Sea, and suggested that these waters provided a significant portion of the salt that helps to maintain the Atlantic overturning. Evaluating the magnitude of this effect has proved difficult. Artale et al. (2002) used a simple two-dimensional model to show that including a salinity perturbation that mimicked that associated with the Mediterranean outflow tended to drive the system towards a more

realistic state. However, Sarnthein et al. (1994) report changes in Mediterranean outflow that are largely independent of the global overturning rate. Results from more realistic models have not yielded a clear picture. One reason for this is that the representation of the Mediterranean outflow in coarse-resolution ocean models has been very unrealistic, treating the flow either in terms of a mixing of properties across the straits of Gibraltar (as in the CM2 model series) or by opening the straits much wider than in real life (as in the NCAR coupled model). Moreover, coarse-resolution level coordinate ocean models suffer from the inability to resolve the frictional bottom boundary layers that move fluid along the bottom (Winton et al., 1998). As noted in Section 2, the isopycnal model used here does not suffer from these deficiencies.

Our runs demonstrate that the location of the Mediterranean outflow within the water column can have an impact on the overturning. A careful examination of the salinities shown in Figure 10a shows that the decrease in salinity between the *Blue* and *Green* runs along the 36.69 isopycnal is far from uniform- along the western boundary of the Atlantic salinity actually increases and the southward flow increases. As shown in Figure 10b, the reason for this can be traced to increased salinities in waters at shallower depths which are advected into the Nordic Seas. The result is to increase the flow through the Denmark Straits and on into the Deep Atlantic.

4. Conclusions

We have demonstrated that insofar as ocean biology affects water clarity, it is far from being a purely passive player in the global climate system. Changing water clarity

can produce significant changes in the climate and circulation, with atmospheric teleconnections linking changes in water clarity to changes in circulation in different basins. A particularly interesting change is that linked to the outflow from the Mediterranean basin- which relies on physics that are much better represented in the isopycnal model used in this study than in the level-coordinate that are typically used in coupled climate model studies.

The sensitivity of the results to shortwave absorption in regions with relatively low levels of chlorophyll further highlights the importance of properly understanding the dynamics of light absorption in these regions. By and large, parameterizations of water clarity have tended to use chlorophyll-a (Morel, 1988), in large part because in-situ measurements of this quantity are relatively easy to make. However, it has become abundantly clear in recent years that a significant fraction of shortwave absorption is due to constituents such as chromophoric dissolved organic matter (Siegel and Dickey, 1996; Siegel et al., 2005; Nelson et al. 2007) which can have radically different behavior than chlorophyll-a.

These simulations also have some important implications for the role of near-surface mixing in climate models. Changing the profile of solar absorption can be seen as similar in effect to changes in the background mixing coefficient, moving heat up and down in the water column. One can get a rough sense of how important this is by computing the diffusive coefficient required to match the additional shortwave flux

$$K_v^{add} = \Delta SW / (\rho c_p \partial T / \partial z) \quad (2)$$

Where ΔSW is the change in downwelling shortwave flux, ρ is the density, c_p is the specific heat and $\partial T / \partial z$ is the background stratification. This quantity was computed for

the Green run, and some cross-sections are shown in Figure 11, taking the difference in shortwave flux as that between the flux associated with *Blue* and a constant e-folding depth of 17m, as in the work of Murtugudde et al. (2003). The additional diffusion required is extremely small, (of order 0.05-0.2 cm²/s) particularly in the shadow zones. This raises some interesting issues about mixing immediately below the mixed layer base. Most coupled models, including ours, assume that once outside the zone of active mixing, the mixing coefficient drops to values typical of the interior (0.1-0.15 cm²/s). However, it is known that the zone immediately below the mixed layer has different internal wave properties and could therefore exhibit different mixing behavior. For example, Anis and Singhal (2006) show microstructure measurements in a freshwater lake in which the pycnocline was well defined. While they do see a marked difference between high mixing coefficients within the mixed layer, they also find patches of high vertical diffusion below this layer. Our results suggest that much more attention be paid to this question.

It is worth discussing what sorts of mechanisms could lead to the large changes in color described here. While the Blue run is clearly unreasonable, significant changes in particulate export have been suggested to occur in a number of locations (Paytan and Griffith, 2007). Analysis of interannual variability in the SeaWiFS chlorophyll-a retrievals from 1998-2004 shows that even over this relatively small period, a range in variation of 40% of the mean is found over 40% of the ocean, with some of the locations with the largest variation occurring along the boundary between the gyres and the shadow zones. One of the most intriguing mechanisms that could account for changes in chlorophyll is changes in iron supply. Iron is an important micronutrient for

phytoplankton, with iron-containing enzymes playing a key role in cellular assimilation of both carbon (through photosynthesis) and nitrogen (through nitrate reduction). Iron supply to the oceans is largely associated with airborne mineral dust, with the Sahara accounting for a large fraction of this supply (Li et al., subm.). These dust sources have changed markedly over time- particularly as a result of Saharan desertification.

Additionally, increases in sulfur dioxide pollution (which as discussed in Fan et al., 2006 acts to increase the solubility of iron in dust) would be expected to increase chlorophyll concentrations in the North Pacific- which as made clear here is one of the key regions where ocean water clarity can affect the Hadley circulation. The impact of such perturbations through their effect on ocean color is another area which this work strongly suggests could be important.

Acknowledgements: The authors thank the Geophysical Fluid Dynamics Laboratory for support of these runs. WGA was supported by NASA under the ECCO consortium (Grant NNG06GC28G) and the Interdisciplinary Science initiative (Grant NNX07AL801G).

We thank Steve Griffies, Laura Jackson and Andrew Wittenberg for reviewing this manuscript, Bonnie Samuels for help with the model setup and for running the control simulation, and Bob Hallberg, John Dunne, and Tony Rosati for useful discussions.

References

- Anderson, W.G., A. Gnanadesikan, R.W. Hallberg, J.P. Dunne and B.L. Samuels, Impact of ocean color on the maintenance of the Pacific Cold Tongue, *Geophys. Res. Lett.*, 34, L11609, doi:10.1029/2007GL030100, 2007.
- Anderson, W.G., A. Gnanadesikan, A. Wittenberg and G.A. Vecchi, What changing ocean water clarity can tell us about tropical variability, in prep. *J. Climate*.
- Anderson, W.G., A. Gnanadesikan, and G.A. Vecchi, Ocean water clarity and tropical cyclogenesis, in prep. for *Nature*.
- Anis A., and M.A. Singhal, Mixing in the surface boundary layer of a tropical freshwater reservoir, *J. Marine Systems*, 63,225-243, 2006.
- Artale, V., S. Calmanti and A. Sutera, Thermohaline circulation sensitivity to intermediate-level anomalies, *Tellus A*, 54, 159-174, 2002.
- Delworth, T. and coauthors, GFDL's CM2 global coupled climate models: Part 1- Formulation and simulation characteristics, *J. Climate*, 19, 643-674, 2006.
- Fan, S.M., W.J. Moxim and H. Levy II, Aeolian input of bioavailable iron to the ocean, *Geophys. Res. Lett.*, 33, L07062, doi:10.1029/2005GL024852,2006.
- Gnanadesikan, A., A simple theory for the structure of the oceanic pycnocline, *Science* 283, 2077-2079, 1999.
- Gnanadesikan, A., and co-authors, GFDL's CM2 global coupled climate models: Part II- The baseline ocean simulation, *J. Climate*, 19, 675-697, 2006.
- Gnanadesikan A. and R.W. Hallberg, On the relationship of the Circumpolar Current to Southern Hemisphere winds in large-scale ocean models, *J. Phys. Oceanogr.*, 30:2013-2034, 2000.

- Harrison, M.J. and R.W. Hallberg, Impact of low equatorial mixing on the tropical circulation in a coupled climate model, in rev. for *J. Phys. Oceanogr.*
- Legaigne, M., C. Menkes, O. Aumont, T. Gorgues, L. Bopp, J.-M. Andre and G. Madec, Influence of the oceanic biology on the tropical Pacific climate in a coupled general circulation model, *Clim. Dyn.*, 28, 503-516, 2007.
- Lewis, M. R., M. E. Carr, G. C. Feldman, W. Esaias, and C. McClain, Influence of penetrating solar radiation on the heat budget of the equatorial Pacific Ocean, *Nature*, 347, 543– 545, 1990.
- Manizza, M., C. Le Quere, A. J. Watson, and E. T. Buitenhuis ,Bio-optical feedbacks among phytoplankton, upper ocean physics and sea-ice in a global model, *Geophys. Res. Lett.*, 32, L05603, doi:10.1029/2004GL020778, 2005.
- Milly, P.C.D. and A.B. Shmakin, Global modeling of land, water, and energy balances, *J. Hydrometeorol.*, 3, 283-299, 2002.
- Morel, A., Optical modeling of the upper ocean in relation to its biogenous matter content (case-I waters), *J. Geophys. Res.*, 93, 10,749–10,768, 1988.
- Murtugudde, R., J. Beauchamp, C. R. McClain, M. Lewis, and A. Busalacchi Effects of penetrative radiation on the upper tropical ocean circulation, *J. Climate*, 15, 470–486, 2002.
- Nakamoto, S., S. P. Kumar, J. M. Oberhuber, J. Ishizaka, K. Muneyama, and R. Frouin, Response of the equatorial Pacific to chlorophyll pigment in a mixed layer isopycnal ocean general circulation model, *Geophys. Res. Lett.*, 28, 2021– 2024, 2001.

- Nelson, N.B., D.A. Siegel, C.A. Carlson, C. Swan, W.M. Smethie and S. Khatiawala, Hydrography of chromophoric dissolved organic matter in the North Atlantic, *Deep Sea Res. I*, 54, 710-731, 2007.
- Paytan, A. and E.M Griffith, Marine barite-recorder of variations in ocean export productivity, *Deep Sea Res. II*, doi:10.1016/j.dsr2.2007.01.007, 2007.
- Reichler, T. and J. Kim, How well do coupled climate models simulate today's climate? subm. *Bull. Amer. Met. Soc.*
- Reid, J.L., On the contribution of the Mediterranean outflow to the Norwegian-Greenland Sea, *Deep Sea. Res.*, 26A, 1199-1219, 1979.
- Sarnthein, M., K. Winn, S.J.A. Jung, J.C. Duplessy, L. Labeyrie, H. Erlenkeuser and G. Ganssen, Changes in east Atlantic deep water circulation over the last 30,000 years- 8 time slice reconstructions, *Paleoceanography*, 9, 209-267, 1994.
- Schneider, E., and Z. Zhu Sensitivity of the simulated annual cycle of sea surface temperature in the equatorial Pacific to sunlight parameterization, *J. Climate*, 11, 1932– 1950, 1998.
- Shell, K. M., S. Nakamoto, and R. C. Somerville, Atmospheric response to solar radiation absorbed by phytoplankton, *J. Geophys. Res.*, 108(D15), 4445, doi:10.1029/2003JD003440, 2003.
- Siegel, D. A., R. R. Bidigare, and Y. Zhou, Solar radiation, phytoplankton pigments and the radiant heating of the equatorial Pacific warm pool, *J. Geophys. Res.*, 100, 4885– 4891, 1995.
- Siegel, D.A., S. Maritorona, N.B. Nelson and M. J. Behrenfeld, Independence and interdependencies among global ocean color properties: Reassessing the bio-

- optical assumption, *J. Geophys. Res.*, 110, C07011, doi:10.1029/2004JC002527, 2005.
- Siegel, D.A. and A.F. Michaels, Quantification of non-algal light attenuation in the Sargasso Sea: Implications for biogeochemistry and remote sensing, *Deep Sea Res. II*, 43, 321-345, 1996.
- Stramska, M., and T. D. Dickey, Phytoplankton bloom and the vertical thermal structure of the upper ocean, *J. Mar. Res.*, 51, 819– 842, 1993.
- Sweeney, C., A. Gnanadesikan, S.M. Griffies, M.J. Harrison, A. Rosati, and B.L. Samuels, Impacts of shortwave penetration depth on large-scale ocean-circulation and heat transport, *J. Phys. Oceanogr.*, 35(6), 1103-1119, 2005.
- Toggweiler, J.R., J. L. Russell, and S. R. Carson, Midlatitude westerlies, atmospheric CO₂, and climate change during the ice ages. *Paleoceanography*, 21, PA2005, doi:10.1029/2005PA001154, 2006.
- Toggweiler, J.R. and B.L. Samuels, Is the magnitude of the deep outflow from the Atlantic Ocean actually governed by Southern Hemisphere winds? In *The Global Carbon Cycle*, Springer-Verlag, 303-331, 1993.
- Toggweiler, J. R., and B. Samuels, On the ocean's large-scale circulation near the limit of no vertical mixing. *J. Phys. Oceanogr.*, **28(9)**, 1832-1852, 1998.
- Winton, M., R.W. Hallberg and A. Gnanadesikan, Simulation of density-driven downslope flow in z-coordinate ocean models, *J. Phys. Oceanogr.*, 28, 2163-2174, 1998.

Property	<i>Green</i> (Isopycnal)	CM2.0 (Level)	CM2.1 (Level)
RMS SST Error Global	1.42	1.49	1.23
90S-30S	1.58	1.31	1.42
30S-30N	1.26	1.05	1.04
30N-90N	1.62	2.60	1.41
RMS Temperature Error 0-1500m	1.31	1.71	1.42
Mean SSS Bias	-0.48	-0.43	-0.20
RMS SSS Error	0.99	1.04	0.87
RMS Salinity Error 0-1500m	0.38	0.37	0.33
SST Bias 180W-100W, 2S-2N	0.28	-0.90	-0.70

Table 1: Control model compared with GFDL's two global coupled climate models run for the Fourth Assessment report.

	Green	Blue	Limit 0.2	Half
Gibraltar Exchange (Sv)	1.82	1.59	1.74	1.71
Inflow salinity	37.11	36.98	37.02	37.09
Outflow salinity	37.66	37.43	37.47	37.60
Gibraltar inflow	0.032	0.015	0.019	0.021
Bosphorus inflow	0.011	0.020	0.014	0.015
Net PME, Med.	-0.043	-0.035	-0.034	-0.037
Nile	0.016	0.020	0.022	0.021

Table 2: Mediterranean salt and water budgets

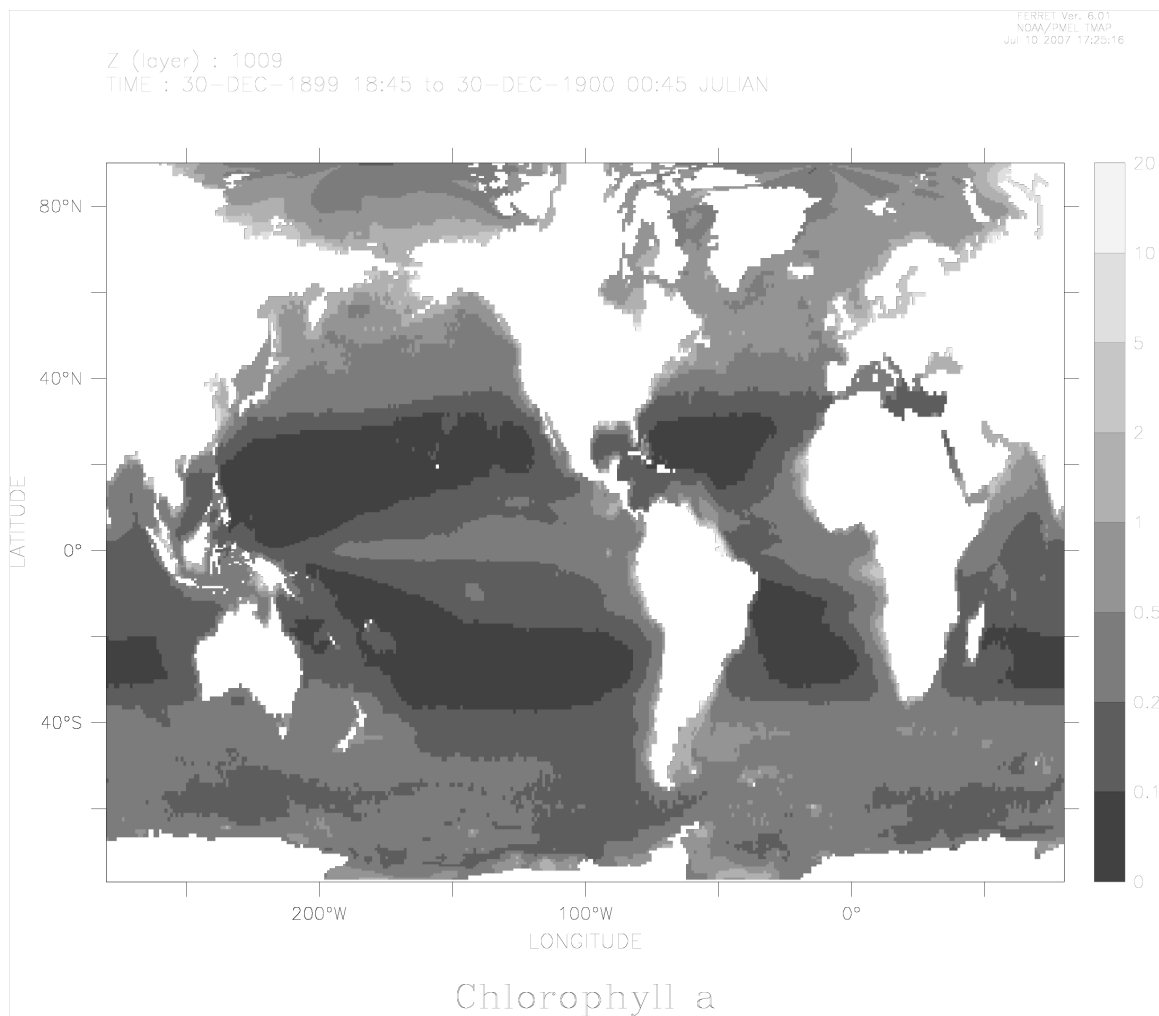


Figure 1: Chlorophyll-a concentrations in mg/m^3 on a logarithmic scale.

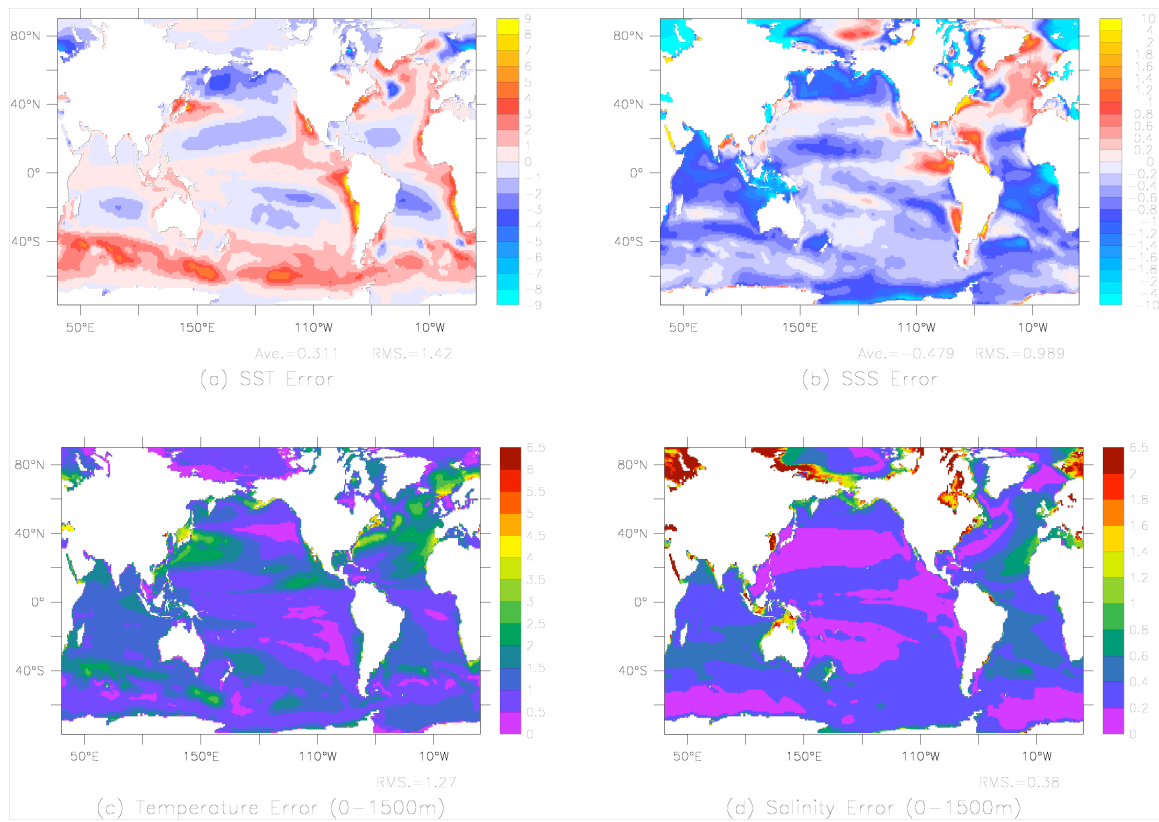


Figure 2: Errors (compared with the World Ocean Atlas regrided to the model grid) in the control simulation averaged over years 200-300. (a) Sea surface temperature in °C. (b) Sea surface salinity in PSU. (c) RMS error in temperature (°C) 0-1500m. (d) RMS error in salinity (PSU) 0-1500m.

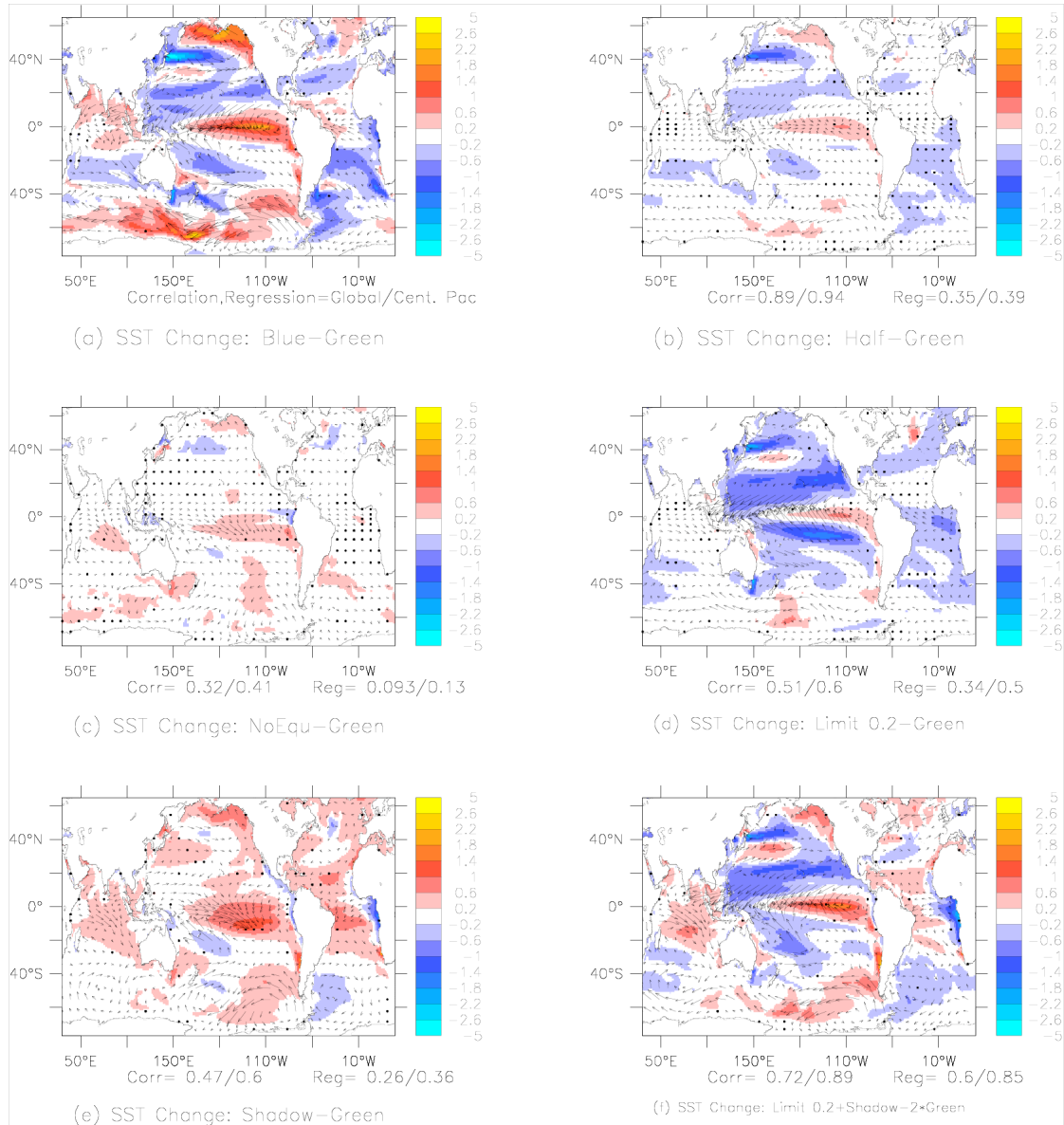


Figure 3: Sea surface temperature ($^{\circ}\text{C}$) and wind stress changes from changing ocean water clarity for years 41-120. Numbers show the correlation and regression coefficients vs. the *Blue-Green* difference- enabling evaluation of which regions are most important for producing the changes in the *Blue* run. (a) *Blue-Green*. (b) *Half-Green* (c) *NoEqu-Green* (d) *Limit_02-Green* (e) *Shadow-Green* (f) (*Shadow-Green*)+(Limit 0.2 –*Green*).

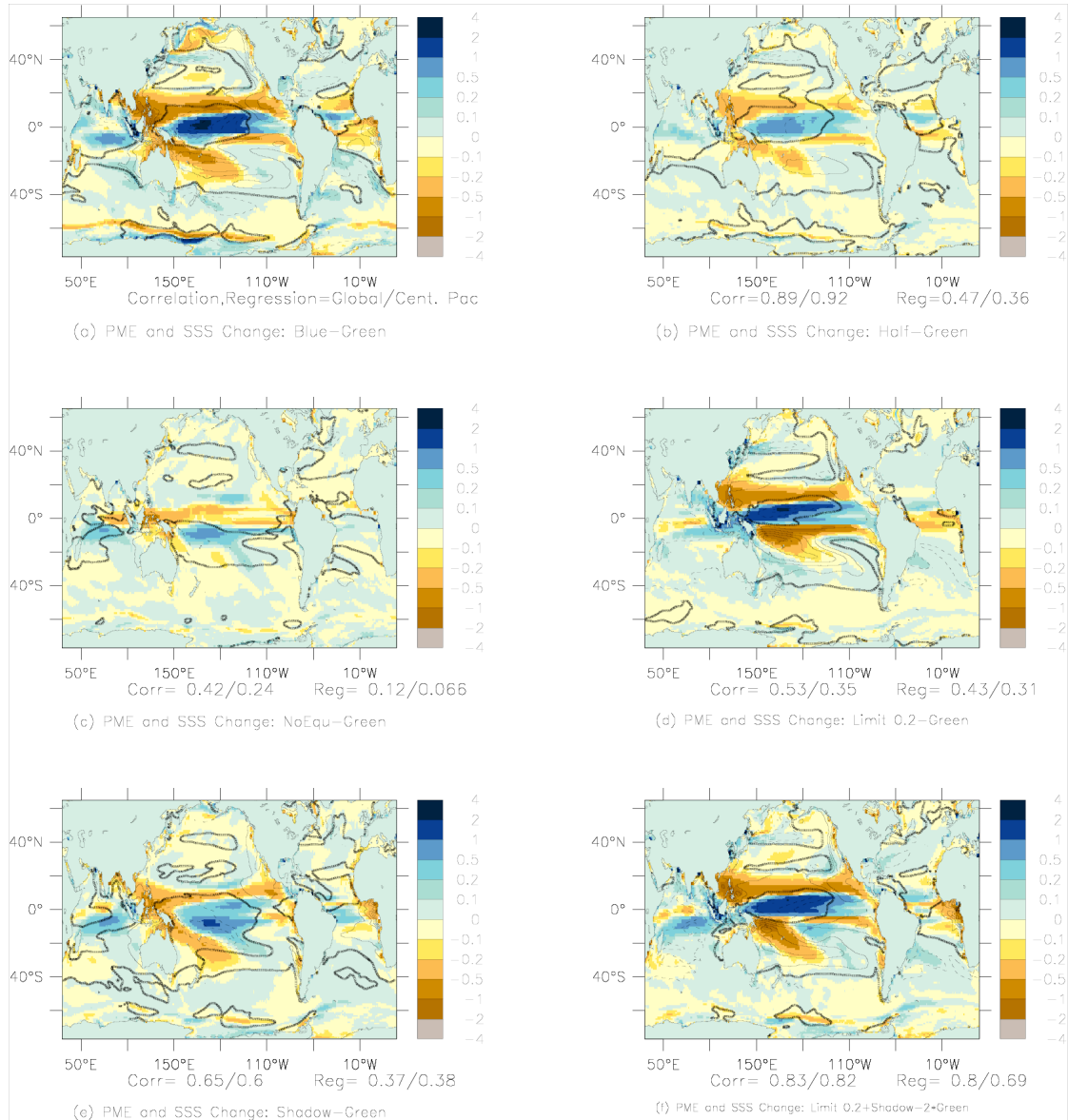


Figure 4: Precipitation-Evaporation (in m/yr, colors) and sea surface salinity (contours, interval 0.2 PSU) changes relative to *Green* run for years 41-120 of the simulations. Correlation and regression coefficients of the change compared with Blue-Green are shown by the numbers below each plot. (a) *Blue-Green*. (b) *Half-Green* (c) *NoEqu-Green* (d) *Limit_02-Green* (e) *Shadow-Green* (f) (*Shadow-Green*)+(Limit 0.2 –*Green*).

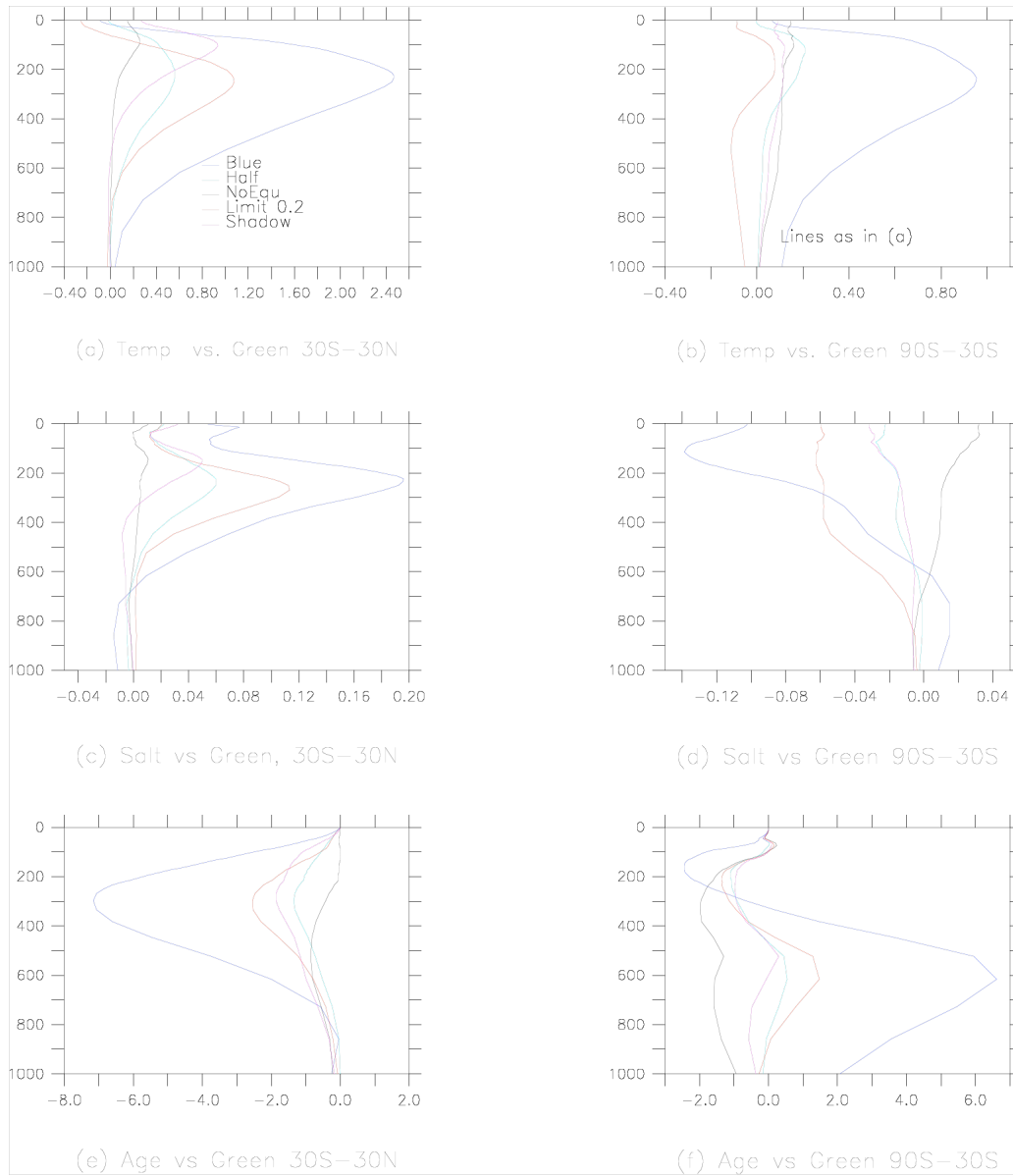


Figure 5: Upper ocean changes in temperature ($^{\circ}\text{C}$), salinity (PSU) and ideal age (years) over resulting from changes in ocean water clarity for years 81-120 of the simulations.

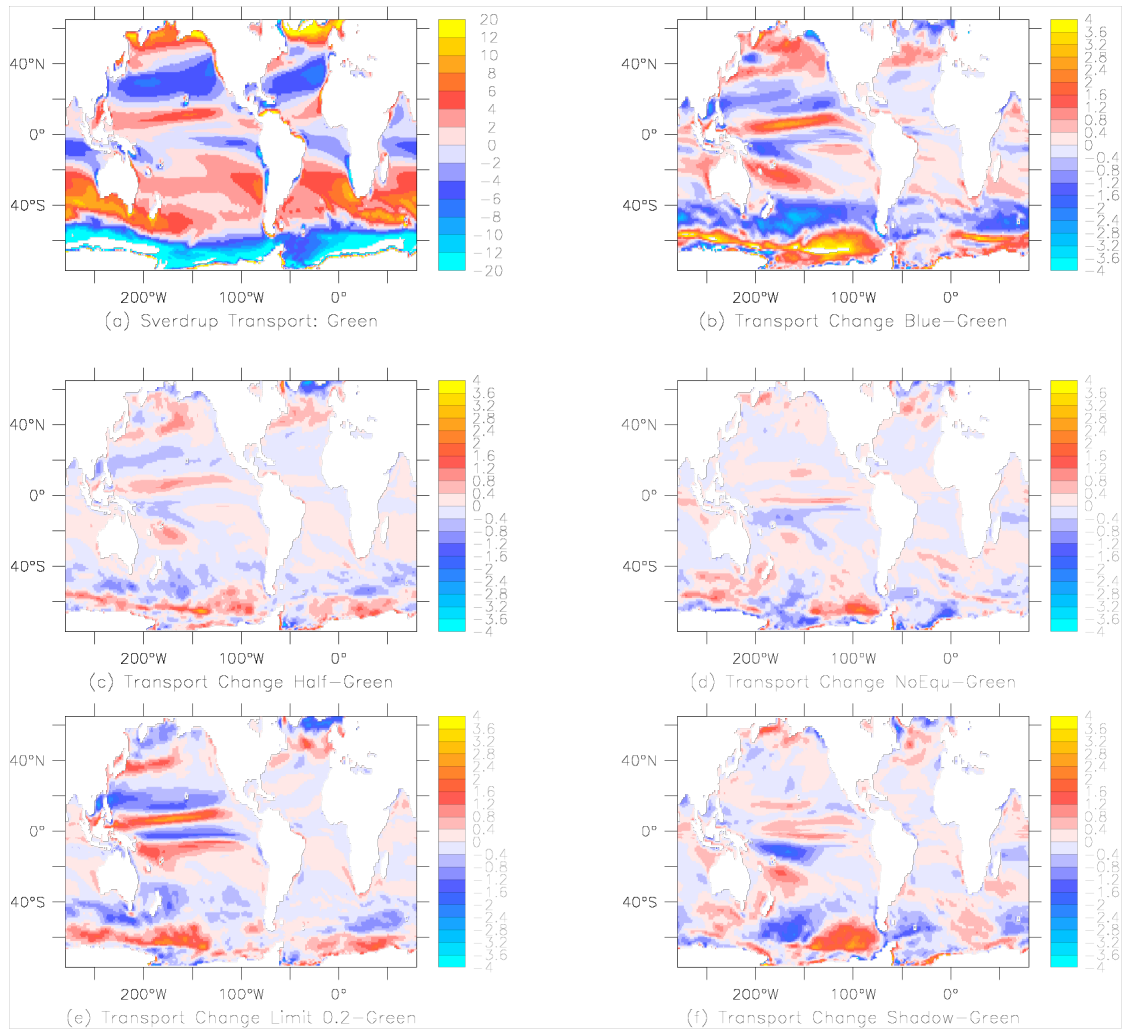


Figure 6: Sverdrup transport and its changes in the model suite for years 41-120 of the simulations. (a) Control transport from Green run. *Green*. Changes in transport are shown for (b) *Blue-Green* (c) *Half-Green* (d) *NoEqu-Green* (e) *Limit_02-Green* and (f) *Shadow-Green*

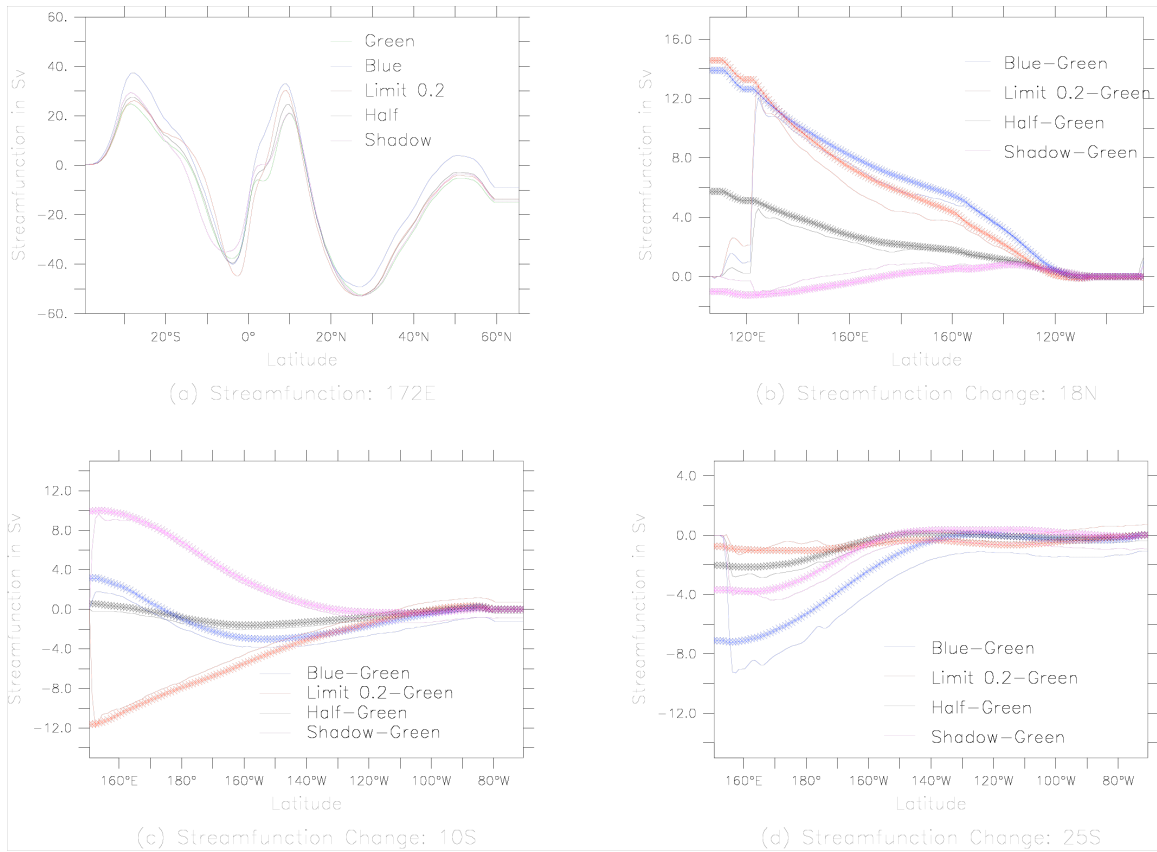


Figure 7: Change in horizontal circulation associated with water clarity changes, symbols show integrated Sverdrup flux. (a) Eastward transport integrated along 172E for four different models. (b) Northward transport integrated across the Pacific at 18N. (c) Northward transport integrated across the Pacific at 10S. (d) Northward transport integrated across the Pacific at 25S.

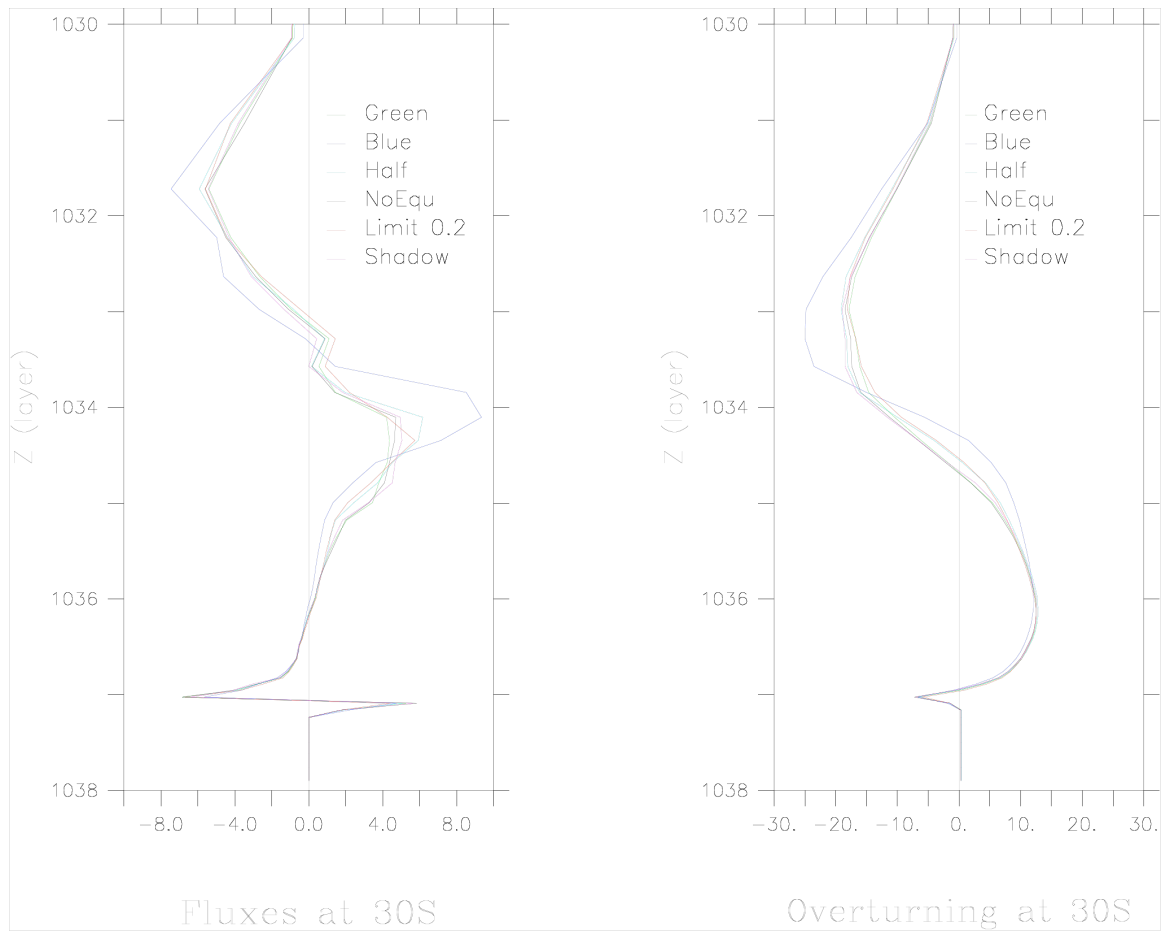


Figure 8: Overturning at 30S. Left: Fluxes in each density class in Sv. Right:

Overturning streamfunction in Sv.

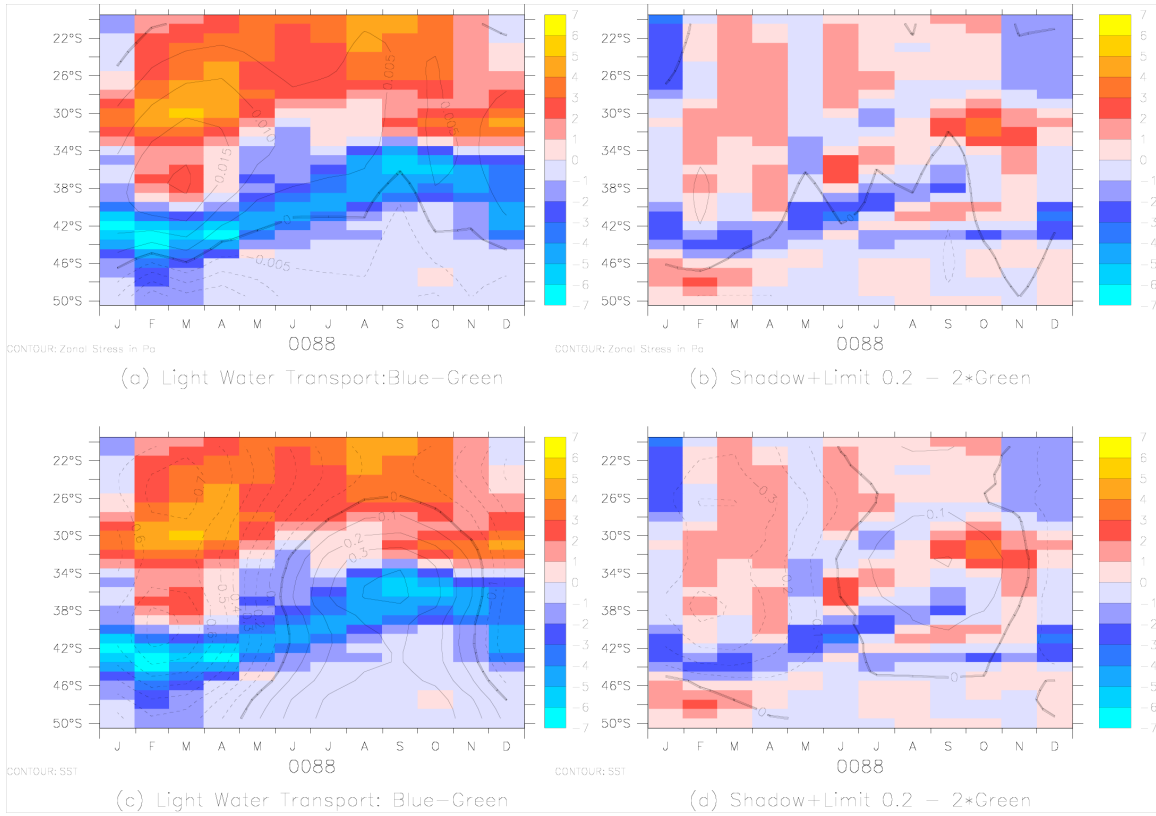


Figure 9: Changes in the northward transport of light water related to surface quantities over the course of the year. (a) Zonally integrated light water transport change in Sv (colors) and zonally averaged surface wind stress change in Pa (contours) between the *Blue* and *Green* runs. Note how light water transport change follows wind stress changes. (b) Same as (a) but for (*Limit 0.2-Green*) + (*Shadow - Green*). Note that the additional northward transport is not seen, nor are the changes in zonally integrated wind stress. (c) Same as (a) but with contours of zonally averaged SST change overlaid. (d) Same as (b) but with contours of zonally averaged SST change overlaid.

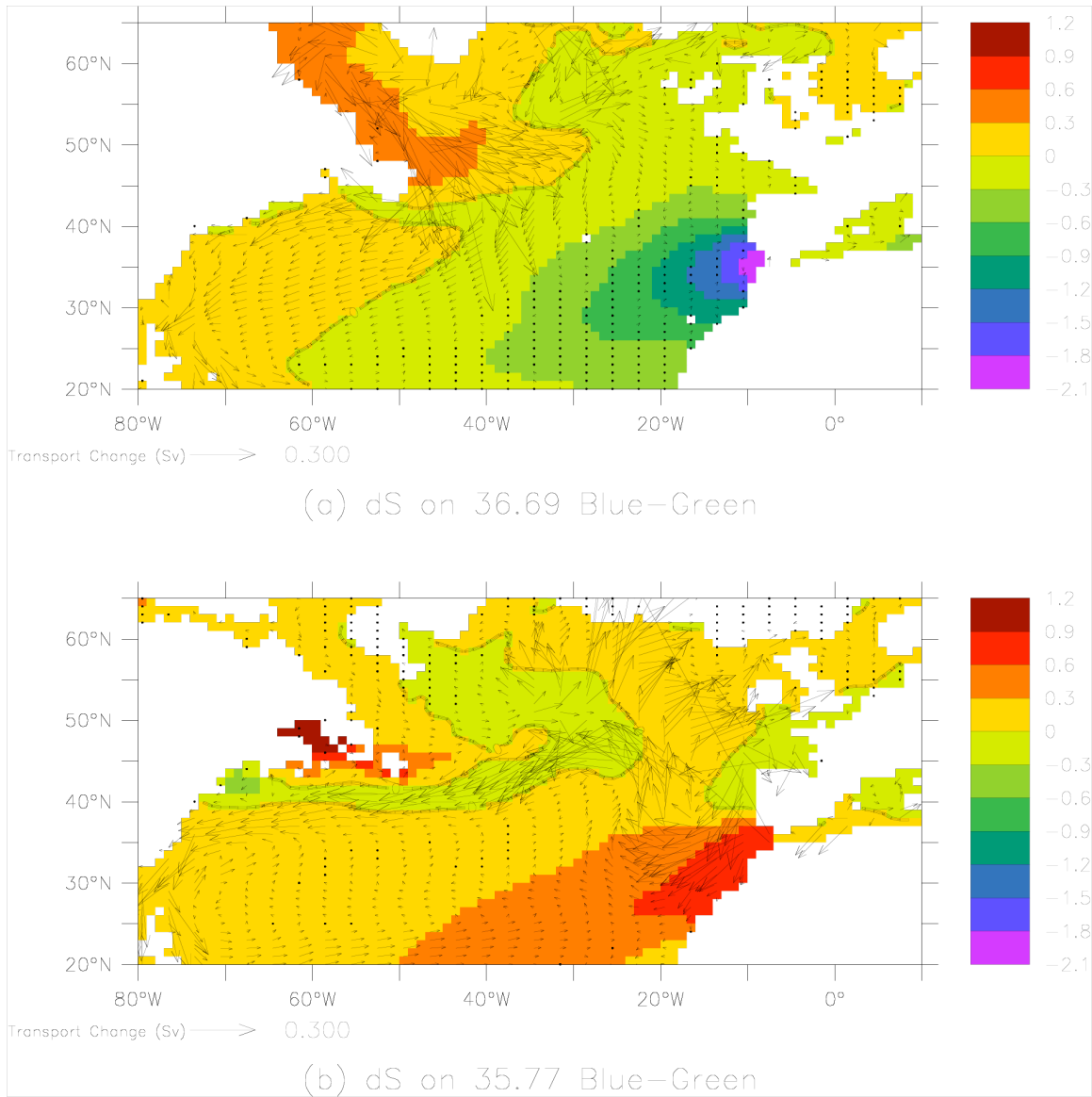


Figure 10: Change in salinity and transport between the *Blue* and *Green* model runs along two layers in the North Atlantic. Salinity decrease near Gibraltar at depth and increase above that is the signature of the diversion of the Mediterranean outflow to lighter densities. Increase in southward transport at depth along the North American coast is balanced by an increased inflow of saltier water to the Norwegian seas. (a) $\sigma_2=36.69$ a layer which lies below the bulk of the pycnocline. (b) $\sigma_2=35.77$ a layer which lies within the pycnocline.

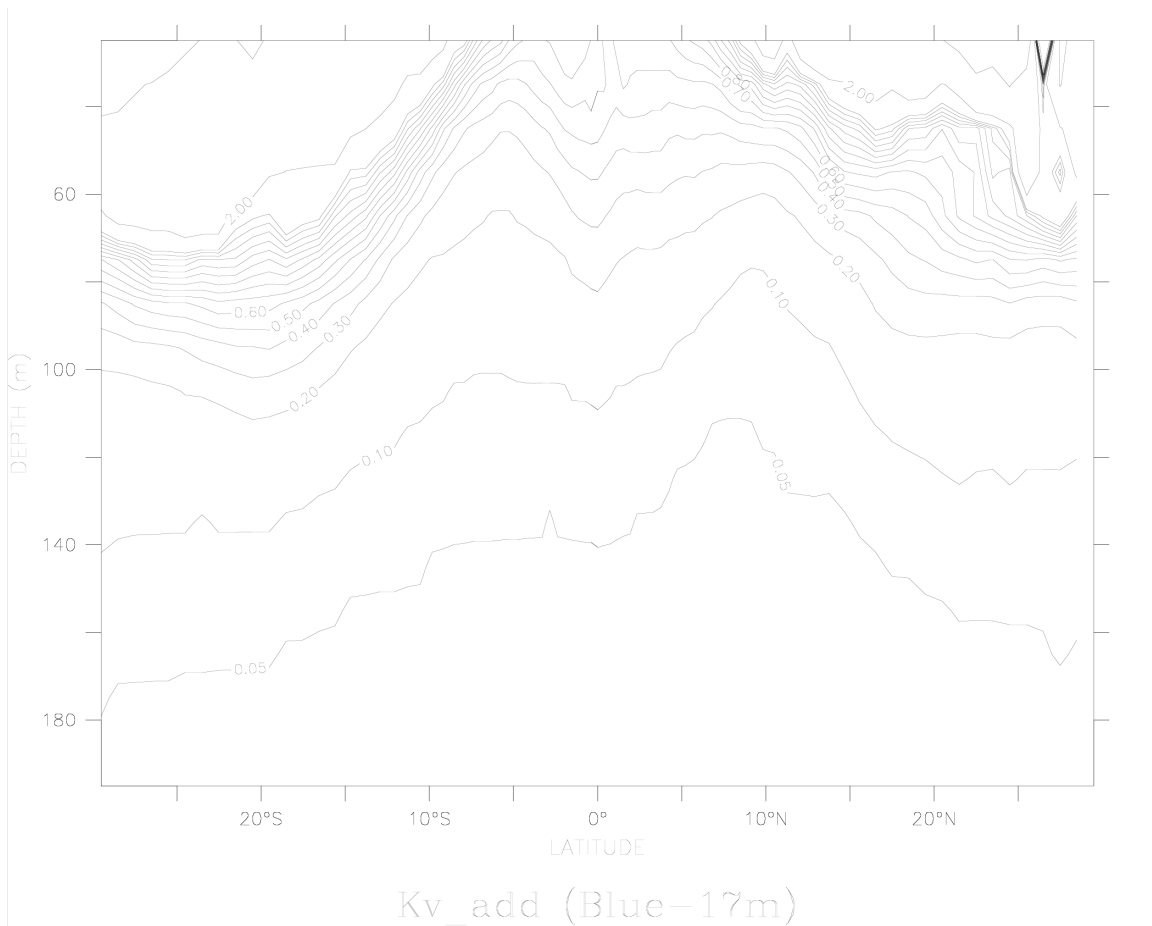


Figure 11: Diffusion coefficient (in cm^2/s) that would produce a heat flux equivalent to the additional shortwave flux caused by changing a 17m e-folding depth for blue light alone to clear water.